Chemistry–A European Journal
Research Article
doi.org/10.1002/chem.202400433
Chemistry Europe
European Chemical Societies Publishing
www.chemeurj.org

Hot Paper

# Synthesis, Structure and (Photo)Catalytic Behavior of Ce-MOFs Containing Perfluoroalkylcarboxylate Linkers: Experimental and Theoretical Insights

Diletta Morelli Venturi,[a, b] Maria Sole Notari,[c] Letizia Trovarelli,[c] Edoardo Mosconi,[d, e] Asma A. Alothman,[e] Anastasia Molokova,[f] Niklas Ruser,[a] Christoph Meier,[a] Bastian Achenbach,[a] Kirill A. Lomachenko,[f] Tiziana del Giacco,*[c] Ferdinando Costantino,*[c] and Norbert Stock*[a, b]

Cerium-based Metal-Organic frameworks (Ce-MOFs) are attracting increasing interest due to their similar structural features to zirconium MOFs. The redox behavior of Ce(III/IV) adds a range of properties to the compounds. Recently, perfluorinated linkers have been used in the synthesis of MOFs to introduce new characteristic into the structure. We report the synthesis and structural characterization of Ce(IV)-based MOFs constructed using two perfluorinated alkyl linkers. Their structure, based on hexanuclear $Ce_6O_4(OH)_4^{12+}$ clusters linked to each other by the dicarboxylate ions, has been solved ab-initio from X-ray powder diffraction data and refined by the Rietveld method. The crystallization kinetics and the MOF formation mechanism was also invesitigated by Synchrotron radiation with XAS spectroscopies (EXAFS and XANES). The MOFs present the same **fcu** cubic topology as observed in MOF-801 and UiO-66, and they showed good stability in water at different pH conditions. The electronic structure of these MOFs has been studied by DFT calculations in order to obtain insights into the density of states structure of the reported compounds, resulting in band gaps in the range of 2.8–3.1 eV. Their catalytic properties were tested both thermally and under visible light irradiation for the degradation of methyl orange (MO) dye.

## Introduction

Metal-Organic Frameworks (MOFs) are crystalline materials formed by inorganic nodes linked to each other by polyfunctional organic molecules. The ability to design and use different Secondary Building Units (SBUs) and ditopic or polytopic organic linkers results in the construction of a large diversity of MOFs whose composition and properties can be adapted to specific applications.[1] In terms of stability and structural versatility Zr-based MOFs are today considered as benchmark materials and are used for many applications ranging from gas sorption and separation,[2] catalysis,[3] water harvesting,[4] as carriers for drug delivery[5] and proton conductivity.[6] On the other hand, the chemistry of Ce(IV) MOFs is a relatively new research field[7] which is attracting a growing interest due to the ability of Ce(IV) ions to afford MOFs isostructural to the Zr analogues but also showing additional properties due to the redox activity of the Ce(IV)/Ce(III) couple.[8] In recent years, Ce-MOFs have found potential applications mainly in (photo)redox and electrocatalysis, as sensors, and for adsorbing and separating gases.[9,10]

The removal of toxic organic contaminants from wastewater, which is necessary to reduce public health hazards and ecosystem damage, has inspired an extensive search for materials capable of efficiently degrading pollutants.[11]

Ce-MOFs are suitable candidates for use as redox (photo)catalysts, as in the recently published results on two isostructural Ce(IV)-MOFs, CAU-58, containing the photoactive

[a] Dr. D. Morelli Venturi, N. Ruser, C. Meier, B. Achenbach, Prof. Dr. N. Stock
Institute of Inorganic Chemistry
Christian-Albrecht University of Kiel
Max-Eyth-Straße 2, 24118 Kiel (Germany)
E-mail: stock@ac.uni-kiel.de

[b] Dr. D. Morelli Venturi, Prof. Dr. N. Stock
Kiel Nano, Surface and Interface Science KiNSIS,
Christian-Albrecht University of Kiel,
Christian-Albrechts-Platz 4, 24118 Kiel (Germany)

[c] M. Sole Notari, L. Trovarelli, Prof. T. del Giacco, Prof. F. Costantino
Department of chemistry, biology and Biotechnology
University of Perugia
Via Elce di Sotto 8, 06123 Perugia (Italy)
E-mail: ferdinando.costantino@unipg.it
tiziana.delgiacco@unipg.it

[d] Dr. E. Mosconi
Computational Laboratory for Hybrid/Organic Photovoltaics (CLHYO),
Istituto CNR di Scienze e Tecnologie Chimiche "Giulio Natta" (CNR-SCITEC),
Via Elce di Sotto 8, 06123 Perugia (Italy)

[e] Dr. E. Mosconi, A. A. Alothman
Chemistry Department, College of Science, King Saud University
11451 Riyadh, Kingdom of Saudi Arabia

[f] Dr. A. Molokova, Dr. K. A. Lomachenko
European Synchrotron Radiation Facility
Avenue des Martyrs 71, 38043 Grenoble Cedex 9 (France)

Supporting information for this article is available on the WWW under https://doi.org/10.1002/chem.202400433

arenedicarboxylic linker molecules 4,4′-oxydibenzoic acid and 4,4′-carbonyldibenzoic acid.[12] Carboxyalkyl linkers have scarcely been described in literature for the preparation of MOFs compared to aromatic ones as the flexibility of the linkers often does not allow to maintain the permanent porosity upon solvent removal.[13,14] However, aliphatic linkers can be used for the preparation of flexible MOFs, able to change their structure upon external stimuli.[15] In literature, examples of the use of such kind of linkers were recently reported such as the Zr-based MOF MIP 203, in which fumaric acid (MIP203-F), succinic acid (MIP203-S) and malic acid (MIP203-M) are employed. Based on the linker used, MIP-203 (-F, -S, and -M) show altered selectivities in $CO_2$ adsorption over $N_2$ caused by different flexibility of the linkers.[16] In recent years fluorinated linkers or fluorinated inorganic building units have been extensively used in order to enhance some properties of the MOFs such as the water stability, the compatibility with hydrophobic polymers and selectivity towards important gases such as $CO_2$ and small unsaturated hydrocarbons.[17] Indeed, the presence of the dipole in the C–F bond, due to the high electronegativity and low electric polarizability of fluorine, can produce a variety of characteristics, including specific adsorption sites for polar molecules. We recently reported a fluorinated Zr-MOF based on tetrafluorosuccinic acid ($H_2$TFS) having a structure similar to that of fumarate MOF-801. It was obtained by direct synthesis and by post-synthetic exchange on preformed Zr-MOF-801, resulting in mixed-linker MOFs. A remarkable increase in $CO_2$ adsorption selectivity and heat of absorption was observed due to the favorable interactions of $CO_2$ with fluorine atoms of the chains.[18] In the present work, two new cerium MOFs were synthetized using perfluoroalkyldicarboxylic acids with different carbon chain length as linkers, namely tetrafluorosuccinic ($H_2$TFS) and octafluoroadipic ($H_2$OFA) acids (Figure 1). The syntheses were carried out at room temperature and two materials with good crystallinity were obtained. The MOFs were fully characterized by powder X-Ray diffraction (PXRD), TGA and gas sorption analysis. Synchrotron light radiation was employed to study the in-situ crystallization kinetics and the oxidation state of Ce ions by means of EXAFS analysis. In order to determine the electronic structure of the two MOFs DFT calculations were employed resulting in band-gaps (BG) comprised into the 2.7–3.1 eV range. The electronic structure of pure Zr-MOF containing $TFS^{2-}$ as linker was also calculated resulting in a BG value higher than 5 eV. However, the calculated electronic structure of hypothetical mixed-metal Ce/Zr-MOFs resulted in a BG of about 3 eV, meaning that mixed-metal Ce/Zr-MOF will very likely maintain the photocatalytic properties with an improved thermal stability typical of Zr-MOFs.[19] In the present work the two Ce-MOFs were employed as catalysts, both under irradiation and in the dark, for the degradation in water of the methyl orange (MO) dye at different pH values. CeOFA was found to display the better catalytic performance probably due to its improved stability and to a favorable adsorption of the dye onto the MOF surface.

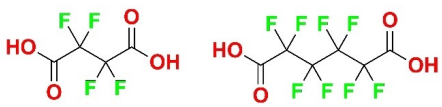


**Figure 1.** Molecular structure of $H_2$TFS (left) and $H_2$OFA (right).

## Experimental Section

### Synthetic Procedures

#### Synthesis of CeTFS $[Ce_6O_4(OH)_4(TFS)_6(H_2O)_4]\cdot 10H_2O$

$(NH_4)_2Ce(NO_3)_6$ (0.4 mmol, 219 mg) and $H_2$TFS (0.4 mmol, 76 mg) were placed together in a 7 ml Pyrex reactor with 1 mL deionized water. The reaction mixture was stirred at room temperature for 1 h. The obtained light yellow solid was recovered by centrifugation, washed twice with water (2 mL) and once with acetone (2 mL) and dried in an oven at 80 °C. ICP analysis: Ce calc 38.67 wt%, exp 35.62 wt%. IR bands ATR ($cm^{-1}$) 3618 (sh), 3577 (br), 1655 (s), 1406 (s), 1175 (s), 1122 (s), 962 (s), 802 (s); Yield 79.4%.

#### Synthesis of CeOFA $[Ce_6O_4(OH)_4(OFA)_6(H_2O)_4]\cdot 7H_2O$

$(NH_4)_2Ce(NO_3)_6$ (0.4 mmol, 209 mg) and $H_2$OFA (0.4 mmol, 106 mg) were placed together in a 7 ml Pyrex reactor with 1 mL deionized water. The reaction mixture was stirred at room temperature for 1 h. The obtained light yellow solid was recovered by centrifugation, washed twice with water (2 mL) and once with acetone (2 mL) and dried in an oven at 80 °C. ICP analysis: Ce calc 30 wt%, exp 27.43 wt%. IR bands ATR ($cm^{-1}$) 3629 (sh), 3577 (br), 1671 (s), 1440 (s), 1164 (s), 1052 (s), 8892 (s), 798 (s); Yield 70.4%.

### In situ Experiment: Synthesis and Combined XAS/XRD Measurements

The in situ study described hereafter took place at beamline ID24-DCM (ESRF, Grenoble, France) and was carried out with SynRAC (**Syn**chrotron-based **R**eaction cell for the **A**nalysis of **C**hemical reactions) unit.[20] The SynRAC unit has been developed for in-situ monitoring of solvothermal synthesis using synchrotron X-ray based techniques. The reaction vessel consists in a 7 mL Pyrex vial placed inside an aluminum casing and is surrounded by a heating mantle for precise control of the temperature. An electromagnetic stirrer is also integrated for sample agitation up to 1200 rpm.

The synthesis of CeTFS and CeOFA were investigate. In a Pyrex reactor, containing 0.4 mmol of linker ($H_2$-TFS 76 mg, $H_2$-OFA 106 mg), 1 mL of a $(NH_4)_2Ce(NO_3)_6$ solution in water (0.4 $mol\cdot L^{-1}$) were injected (20 $mL\cdot min^{-1}$) in order to start the reaction. The experiments were performed at room temperature.

**X**-ray absorption spectroscopy (XAS) data were collected at Ce K-edge. The storage ring was operating in 16-bunch top-up mode with 75 mA maximum current. X-rays were generated by an undulator with 27 mm period (5$^{th}$ harmonic). Rejection of higher harmonics was ensured by a pair of Pt-coated mirrors positioned at 1.8 mrad angle to the incident beam. Energy scanning was done by a fixed-exit monochromator with a pair of Si311 crystals. The spectra were collected in continuous mode and the undulator gap was also scanned in real time in order to match the energy of the monochromator. Detection was done by three ion chambers (OKEN) operated at 2 kV and filled with 30% $Kr/N_2$ ($I_0$) or pure Kr ($I_1$,$I_2$) at 1 bara pressure. Resulting time resolution was around 20 s per spectrum. Collected XAS data were treated using inhouse code relying on Larch Python library.[21]

XRD patterns were collected at 35.1 keV ($\lambda = 0.353$ Å) using a 2D detector (Dectris Pilatus 1 M) placed at a calibrated distance of 75 cm from the reactor. XRD data were integrated using DIOPTAS software,[22] that relies on the PyFAI library.[23] Resulting time resolution was around 7 s per XRD pattern.

In order to increase the time resolution, XAS and XRD data were collected separately, so the synthesis of each MOF was repeated twice in identical conditions.

### DFT Calculation

MOF geometry optimization has been carried out with the CP2 K code.[24] Atom-centered Gaussian-type basis functions were used to describe the orbitals. The MOLOPT[25] basis set for Ce, Zr, O, C, F and H was employed and a cutoff of 500 Ry for the plane waves along with PBE functional was used.[26] Core-valence interactions are described by Goedecker-Teter-Hutter pseudopotentials.[27] In this simulation, the structural data obtained from the Rietveld refinement was used as the initial model and a joint atomic position and cell parameters optimization keeping the three axis orthogonal was performed. The Brillouin zone was sampled at the $\Gamma$ point. Electronic structure calculations were carried out following a similar approach as proposed by Truhlar and co-workers,[8] the electronic properties were calculated with the HSE06 hybrid functional as implemented in the VASP program package.[28,29] As already reported, HSE06 nicely reproduces band gaps of various functionalized Zr-UiO-66[30] and Ce-MOFs,[31] showing quantitative agreement with the experimental values. The core − valence electron interactions were described using the projector augmented wave (PAW) method 3 with electrons from H1s; C 2s2p; N 2s2p; O 2s2p; F 2s2p; Zr 4s4p5s5d; Ce 5s5p6s5d4f shells explicitly included in calculations. Dispersion interaction were described with the DFT-D3 approach.[32,33] Single point calculations on the relaxed geometries were carried with the HSE06 functional.[34]

### Degradation Experiments

For the photocatalytic tests, the suspensions were prepared in a vial by adding 5 mg of the respective MOF (1 $g \cdot L^{-1}$) to 5 mL of the dye aqueous solution ($4 \times 10^{-5}$ M) at different pH values adjusted using either HCl or NaOH. Measurements were carried out in an Applied Photophysics multilamp apparatus equipped with six phosphor-coated fluorescent lamps (15 W each) emitting at 355 nm ($\Delta\lambda_{1/2} = 20$ nm). The two MOFs show absorption in the range of 200 and 450 nm (Figure S1). During the reaction, the suspension was stirred and kept in air and at room temperature. The dye degradation was monitored at different irradiation times. The catalyst was separated by filtration through a 0.20 μm-pore size membrane filter (Minisart RC). The filtrate was transferred into a 4-mL quartz cuvette for UV-Vis analysis. Absorption spectra were recorded on an Agilent 8453 Diode Array UV-Vis spectrophotometer. Observed rate constants were determined by monitoring the change of absorbance at the absorption maximum as a function of the irradiation time. The same procedure was performed to determine the amount of MO degradation under dark conditions.

## Results and Discussion

Crystalline CeTFS and CeOFA are easily synthetized at room temperature without using acidic modulators. The structures were solved ab-initio and refined against powder X-ray diffraction data using the Rietveld method (See SI for details, Figure S3 and S4).

The PXRD patterns were indexed by using the N-TREOR[35] program resulting in cubic unit cells as observed for Zr-MOF-801 ($a = 18.0423(5)$ and 19.8233(4) Å for CeTFS and Ce-OFA, respectively).[18] The increase of lattice parameter value by a factor of more than 1.5 Å compared to the one for CeTFS is in line with the increase of the linker size. The refinements were successfully carried out in the *Pa*-3 space group and for both compounds the same **fcu** topology was observed as for Ce-MOF-801.[7] The Ce atoms form hexanuclear clusters, and they are nine fold coordinated with an apical water molecule, as also found in RE-**fcu** MOFs.[36,37] The hexanuclear clusters are twelve fold connected through the linkers leading to octahedral and tetrahedral pores decorated by the F-atoms. Due to the steric hindrance of the F atoms in CeTFS, the carboxylate groups are in *pseudo*-trans position relative to the central C–C bond. For the same reason, the $OFA^{2-}$ linker in CeOFA is in an extended conformation with the F atoms arranged in a helix to minimize interactions (Figure 2). In comparison to the defect-free frameworks, the Ce content of CeTFS and CeOFA is lower by 3 and 2.6%, respectively. These small deviations have been attributed to missing cluster defects.[38]

The FT-IR spectra confirm the presence of the $\mu_2$-OH group in the hexanuclear $M_6O_4(OH)_4^{12+}$ clusters with the signal are around 3620 $cm^{-1}$.[39] The presence of additional guest molecules such as unreacted linker can be excluded since the C–OH band is not observed. The two bands at around 1660 and 1420 $cm^{-1}$ are related to the symmetric and asymmetric stretching vibration of the carboxylate group that coordinate to the cerium ion. The C–F stretching and deformation bands are also present (Figure S6 and Table S6).[40]

Mercury software was used to perform geometric pore size analysis on both compounds, using helium as the probe. Additionally, a comparison was made with the Ce-fumarate MOF reported in 2015.[7] The accessible pore volume for the Ce-fumarate MOF is about 0.161 $cm^3 g^{-1}$, while the values for CeTFS and CeOFA are 0.141 and 0.136 $cm^3 g^{-1}$, respectively. These values are lower than those measured for Ce-fumarate due to the presence of bulky fluorine atoms.

However, CeTFS and CeOFA have a network accessible surface area of 0 $A^2$, while Ce-fumarate has a value of 15 $A^2$. This indicates that the F atoms of the chain significantly restrict gas diffusion, which is consistent with the very low $N_2$ absorption uptake measured for CeTFS and CeOFA at 77 K. The same behavior has been previously reported for ZrTFS.[18]

Similarly in the analogue ZrTFS,[18] the presence of fluorine atoms on the aliphatic chains reduces the windows size significantly compared to the fumarate based MOF-801 (about 3.2 Å vs 5 Å), preventing the adsorption as demonstrated by the $N_2$ and $CO_2$ absorption measurements at 77 and 298 K, respectively (Figure S9 and S10). The water sorption isotherm shows an uptake of about 15% and 9% at 0.9 $p/p^0$ for CeTFS and CeOFA at 298 K, respectively (Figure S11).

Contrary to the expected behavior, both CeTFS and CeOFA exhibit water absorption even at low relative humidity levels (about 10% at room termperature), suggesting that

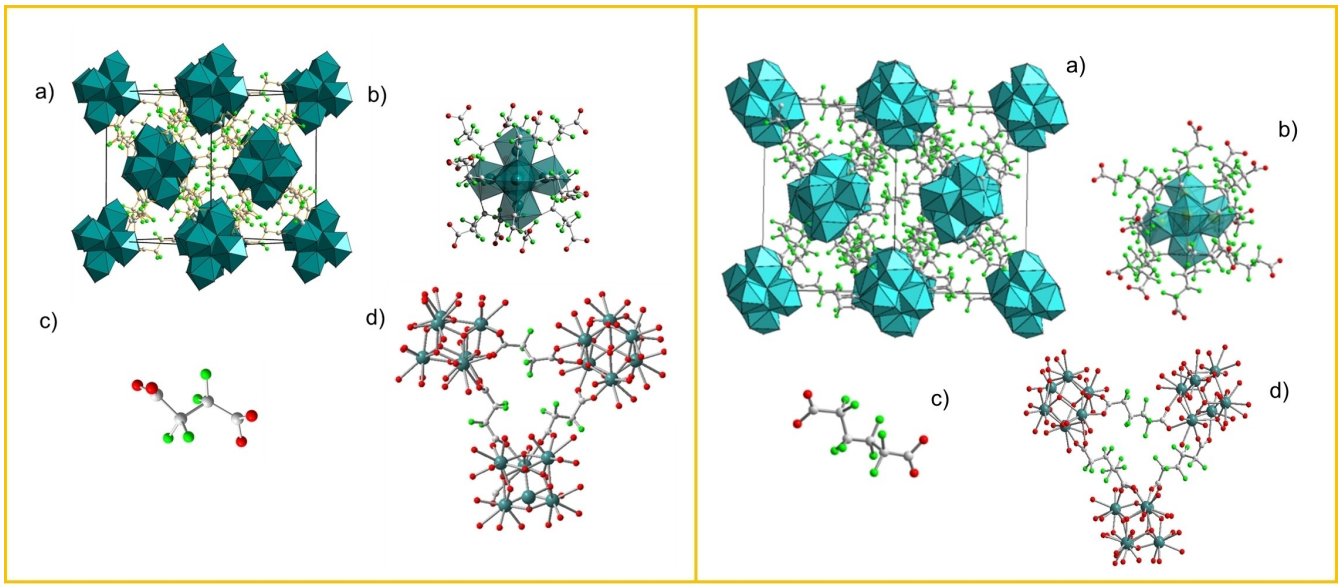


**Figure 2.** Left panel: Polyhedral representation of CeTFS (a), detail of the hexanuclear 12-c cluster (b), of the ligand conformation (c) and detail of the tetrahedral cavities in CeTFS (d). Right panel: Polyhedral representation of CeOFA viewed along [110] (a), detail of the hexanuclear 12-c cluster (b), of the ligand conformation (c) and of the tetrahedral cavity within CeOFA (d).

the pore environment has poor hydrophobicity. In addition, the powders are readily dispersed in water during the catalytic test. According to Mayrhofer et al., the crucial factor for the hydrophobicity of fluorinated materials lies in their ordered structures.[41] Indeed, the intricate hydrophobic properties of fluorinated carbon compounds are due to minimal electrostatic interactions between the surface and water, a phenomenon observed only when the surface is highly ordered. Based on the structures refined from PXRD data, CeTFS and CeOFA exhibit a high degree of linker disorder. Consequently, based on the structure data of the two materials and the model proposed by Mayrhofer et al, it is plausible to correlate the low hydrophobicity of the materials with the structural disorder present.

### In Situ Experiment: Synthesis and Combined XAS/XRD Measurements

Real-time monitoring of the synthesis process was conducted PXRD and Ce K-edge XAS. The XRD patterns collected during the synthesis of CeTFS and CeOFA are presented in Figures S12 and S13. Evolution of the XANES spectra during the synthesis of CeOFA and CeTFS is presented in Figure S14. In order to obtain concentration profiles of the involved Ce species and make sure that the synthesis at the beamline resulted in the same compounds as in the controlled conditions in the lab, linear combination fitting (LCF) of XANES spectra was performed. For each compound two reference spectra were used: the spectrum of aqueous solution of cerium ammonium nitrate (starting material) and the spectrum of the corresponding MOF synthesized in the lab and measured in the solid state as self-supporting pellet (Figure 3a).

Resulting concentration profiles for CeTFS and CeOFA are presented in Figure 3b, c. Notably, for both CeTFS and CeOFA, the conversion of cerium ammonium nitrate to the final products was observed. The reaction kinetics for CeTFS showed a higher reaction rate, achieving complete transformation of CAN in water to the final product in less than 1 minute. In contrast, the reaction rate for CeOFA was significantly slower, with the fraction of the final product reaching approximately 80 % after 15 minutes. The low values and, overall, weak variations of the R-factor confirm the reliability of the fits (fits of the final spectra of each synthesis are presented in Figure S15). Small, but measurable increase of the R-factor in the first minutes of the reaction was found to correspond to the increase of the overall noise of the XANES data, most probably due to the physical inhomogeneity of the solution (Figure S16). Figure 3b, c shows the concentration profiles obtained from LCF together with the evolution of the intensity of the first XRD reflection appearing upon the formation of CeTFS and CeOFA. The two trends observed by XRD and XANES are in good agreement, confirming that the evolution of Ce local environment is directly related to the crystallization of the MOFs.

### DFT Calculations

In order to gain insight into the electronic and optical properties of the new materials, DFT calculations were carried out. In particular, the geometry optimization of the crystal structures and the determination of the density of states (DOS) were carried out for CeTFS, CeOFA and ZrTFS, as well as for a theoretical structure containing mixed-metal Ce/Zr clusters, see ESI for the model details.[18] For ZrTFS a band gap of 5.2 eV was

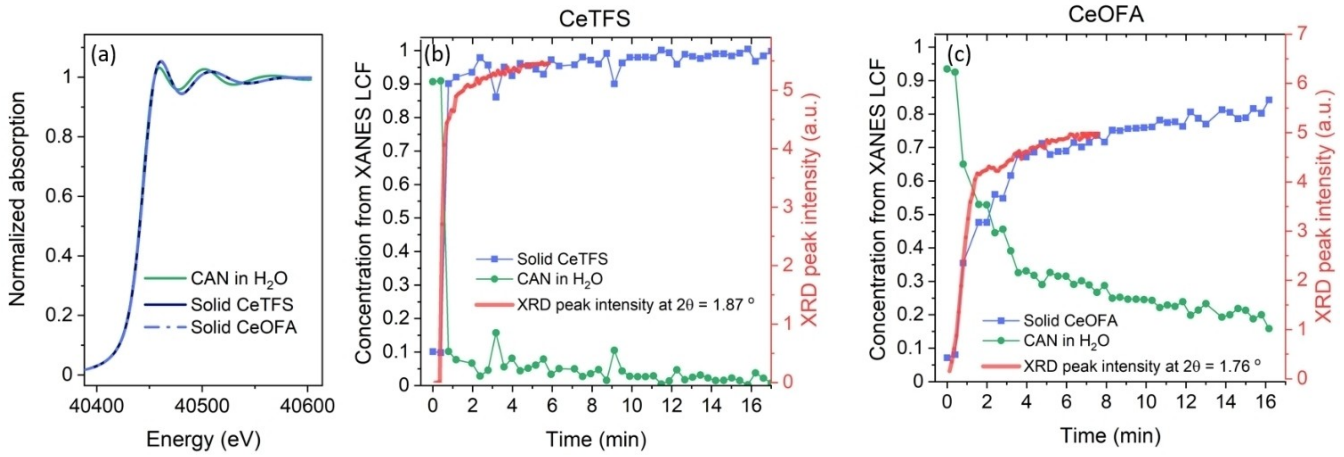


**Figure 3.** (a) Normalized Ce K-edge XANES spectra of references for linear combination fitting (LCF): pellets of CeTFS and CeOFA, and water solution of cerium ammonium nitrate (CAN in $H_2O$); (b, c) Concentration profiles of reference species obtained by LCF of the in situ Ce-K-edge XANES data in comparison with time evolution of the intensity of the first XRD peak of CeTFS (b) and CeOFA (c) structures measured in situ during the synthesis.

found, see Table 1, and the occupied states and the unoccupied states show a similar contribution from both the inorganic cluster and the linkers with a slight predominance of the organic moiety, see Figure S18.

Moving to the mixed Ce/Zr species, a significant change in the DOS was found with the introduction of a new signal related to the unoccupied states, which is associated to the Ce cluster, obtaining a calculated band gap of 3.0 eV, see Table S7 and Figure S18. This behavior is clearly confirmed going to the fully Ce-based species (CeTFS), which shows higher unoccupied Ce-states DOS due the higher Ce content, compared to the mixed Ce/Zr species, with a band gap of 2.8 eV. These values are similar to those previous calculated for other Ce-based MOFs.[31] Finally, for CeOFA, only marginal changes of the band gap energy and the DOS shape are observed in comparison to CeTFS (Table 1, Figure S18).

For photocatalytic applications in general the evaluation of absolute band edge positions (with respect to the vacuum level) and the band gap of the photocatalyst are fundamental to predict the thermodynamic feasibility of the photocatalytic reactions. To assess the potential photocatalytic properties of the investigated materials, the highest occupied crystal orbital (HOCO) energy level was approximated to the HOMO energy of the isolated organic liker bridging two clusters (Figure S19) and the lowest unoccupied crystal orbital (LUCO) energy level is calculated by adding the calculated band gap to the HOCO values. As can be seen in Table 1, there is only a small difference in the HOCO level of clusters bridged by $TFS^{2-}$ and $OFA^{2-}$ ions, with values between −7.1 and −7.3 eV, which in terms of potential corresponds to about 2.4–2.6 V vs. SCE, respectively (conversion as indicate in ref [42]).

**Table 1.** Theoretical highest occupied crystal orbital (HOCO) and lowest unoccupied crystal orbital (LUCO) values along with the calculated band gap (eV).

| compound | HOCO | LUCO | Band Gap |
|---|---|---|---|
| ZrTFS | −7.1 | −1.9 | 5.2 |
| CeTFS | −7.2 | −4.4 | 2.8 |
| CeOFA | −7.3 | −4.4 | 2.9 |
| Ce/Zr cluster | – | – | 3.1 |

## Degradation Experiments

Methyl orange (MO) degradation was chosen as a model pollutant to investigate the catalytic activity of CeTFS and CeOFA in aqueous solution. MO contains a sulfonic acid group, which explains the good solubility of this dye in water. In order to investigate the influence of the degree of deprotonation of the dye on the catalytic activity of the MOFs, the MO degradation was carried out at a fixed MOF/substrate molar ratio (ca. 55 and 71 for CeOFA and CeTFS, respectively, both calculated per Ce atom) at pH 2.5 and 6.7. These values are below and above the $pK_a$ of MO, reported to equal 3.47 in water at 25 °C (Figure S20).[43] At pH 2.5, the UV-Vis spectrum of MO shows two UV absorption bands at 277 and 318 nm due to the $\pi \rightarrow \pi^*$ transitions of the aromatic rings of MO, and a more intense visible band (maximum) at 506 nm due to the $\pi \rightarrow \pi^*$ transition of the azo group (–N=N– bridge). A hypsochromic shift of the absorption bands is observed for the deprotonated form of MO, $\lambda_{max} = 272$ and 465 nm, (Figure S21).[44] A complete degradation of the dye after 60 min at pH 2.5 was found for CeOFA (Figure 4). The time evolution of the spectra shows that the visible band is replaced by an absorption band centered at 250 nm (inset in Figure 4). This clearly shows that intermediates with azo bonds (–N=N–) and their associated chromophores do not accumulate under these experimental conditions. The formation of byproducts containing the aromatic ring is supported by an absorption band with a maximum at 250 nm, which shows that complete decomposition has not yet occurred. MO degradation in the presence of CeOFA performed in the dark gives rise to the time-dependent UV-Vis spectra

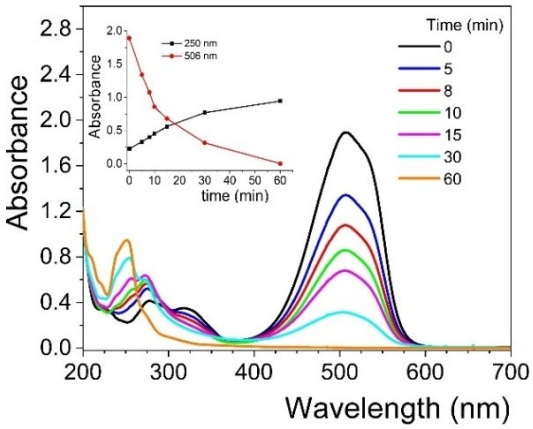


**Figure 4.** Absorption spectra recorded during the photodegradation (λ = 355 nm) of MO ($4.0 \cdot 10^{-5}$ mol·L$^{-1}$) with CeOFA (1.0 g·L$^{-1}$) in aqueous dispersion at pH 2.5 as a function of irradiation time. Inset: change in absorbance at 250 and 506 nm as a function of irradiation time.

depicted in Figure S22. As observed, the spectral shape is similar to that observed under irradiation, but a lower degradation rate was found. Quantitative kinetic analysis was performed with pseudo first-order relation (Equation 1).

$$C = C_0\, e^{-kt} \quad (1)$$

$$k = K \cdot k_r \quad (2)$$

In this equation $k$ is the degradation rate constant, which depends on $K$, the reactant adsorption constant, and $k_r$, the effective reaction rate constant (Equation 2).

Equation 1, derived from the Langmuir–Hinshelwood model, is valid at low substrate concentrations. In addition there is no catalyst saturation and the adsorption of the reaction intermediates can be neglected.[45] By regression of absorbance at 506 nm as a function of time (Figure S23 and S24), the $k$ value under irradiation (0.071 min$^{-1}$, $R^2 = 0.9944$) was calculated which is greater by a factor of ca. 7 compared to the one determined in the dark (0.010 min$^{-1}$, $R^2 = 0.9891$). The reason for the difference in catalytic efficiency may lie in the different nature of the oxidizing sites operating under thermal and photochemical conditions. Metal nodes with coordinatively unsaturated sites or with some exchangeable ligands not involved with in the lattice structure, can act as catalytic centers, analogous to molecular metal complexes used in homogeneous catalysis. Therefore, under thermal conditions, this type of node can promote Lewis acid catalyzed reactions.[46]

The metal nodes of MOFs can also be regarded as isolated semiconductor quantum dots, which can be excited upon light irradiation. The experimental results can be rationalized according to the mechanism depicted in Scheme 1. Excitation with UV light absorbed by the MOF (around 355 nm) promotes the electron transfer from the valence band (VB) to the conduction band (CB) of CeOFA (calculated band gap 2.9 eV, equal to

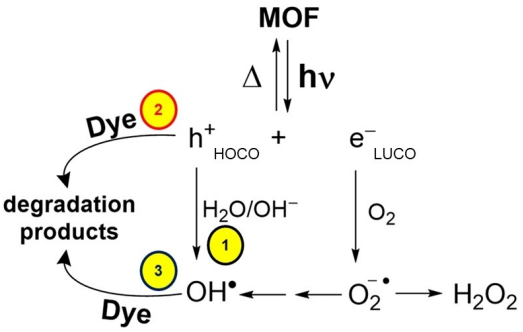


**Scheme 1.** Mechanism of MO degradation photocatalyzed by Ce-MOF (CeTFS and CeOFA). After generation of a hole ($h^+_{HOCO}$) and an electron ($e^-_{LUCO}$) by UV irradiation of the MOF different pathways for dye degradation are possible. (1) Oxidation process of $OH^-$ and $H_2O$ by the holes, (2) MO oxidation by electron transfer to $h^+_{HOCO}$ and (3) MO oxidation by a hydroxyl radical.

433 nm) leading to the generation of a hole ($h^+_{HOCO}$) and an electron, respectively ($e^-_{LUCO}$).

As reported for $TiO_2$, electrons react with $O_2$ to form oxidative species such as $H_2O_2$ and OH$^\bullet$; the latter radicals could also be produced from oxidation of $OH^-$ and $H_2O$ by the holes (**1**), see Scheme 1.[47] The hydroxyl radicals, being highly reactive species, are considered responsible for the more efficient MO degradation under photochemical conditions. However, direct oxidation of the dye by the holes cannot be excluded. Indeed, as shown in Scheme 1, MO can be oxidized by electron transfer to $h^+_{HOCO}$ (**2**) and to hydroxyl radical (**3**) due to its redox potentials (1.02 vs SCE[48] less positive than the CeOFA potential (here calculated 2.6 V vs SCE) and OH$^\bullet$ (2.49 V vs SCE).[49,50]

Finally, in Figure 5, the calculated DOS of CeOFA aligned with MO and OH$^\bullet$ energy level rescaled vs. vacuum is reported (negative values with respect to the potentials rescaled as indicated in ref. [42]). This suggests the possibility of the hole transfer from the MOF to form the hydroxyl radical (**1**, oxidation process of OH$^\bullet$ and $H_2O$) or to directly oxidize the MO (**2**, see Scheme 1 and Figure 5).

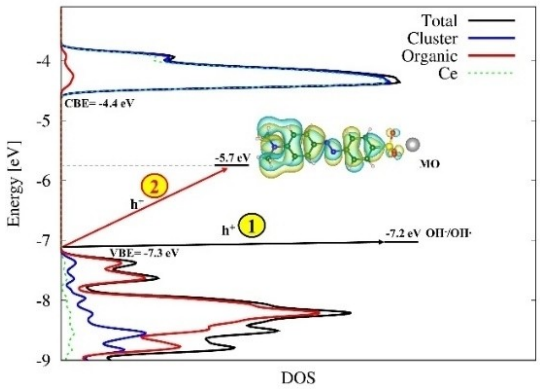


**Figure 5.** Electronic DOS of CeOFA aligned to the MO and OH· potential. The isodensity plot of the HOMO orbital is shown for MO (sodium salt)[47] (1) Oxidation process of OH$^\bullet$ and $H_2O$ by the holes. (2) MO oxidation by electron transfer to $h^+_{HOCO}$.

Experiments carried out in the absence of CeOFA, both under irradiation and in the dark, showed no significant disappearance of MO, therefore the MOF plays a key role in the dye degradation.

The shape of the absorption spectra as a function of time in presence of CeTFS at pH 2.5 (Figure 6) is very similar to that observed with CeOFA under identical experimental conditions (Figure 4). As seen with CeOFA, the decrease in the intensity of the visible band at 506 nm is accompanied by an increase in the intensity of the band at 250 nm (Figure 6). In parallel, a new band is observed at 211 nm, assignable to the formation of aromatic degradation products. As observed for CeTFS, the photocatalyzed degradation was faster than the thermal degradation by a factor of 3 ($k = 0.12\ min^{-1}$ and $0.040\ min^{-1}$, respectively). The kinetic analysis of both reactions and the absorption spectra recorded as a function of time under dark conditions are represented in Figures S21 and S22. As can be seen, the presence of the MOF was essential to be able to observe MO degradation under both irradiation and dark conditions.

Based on the rate constant values, CeTFS appears to be more active than CeOFA in the dye catalyzed degradation. This effect can be attributed to the electron withdrawing substituents, since the F atoms increase the Lewis acidity and thus the oxidizability of the metal nodes (although very close VBE level values were calculated for the two MOFs, see Table 1). The higher activity of CeTFS could also be explained by the lower steric hindrance of the fluorine atoms surrounding the $Ce_6O_4(OH)_4^{12+}$ clusters, which would favour the access of the dye to the oxidative sites. Thus, the higher reactivity of this MOF is probably due to steric hindrance rather than electronic effects. This is also in line with the similar electronic structure, VBE level and band gap calculated for CeTFS and CeOFA species.

A significant difference in degradation kinetics at pH 6.7 compared to the more acidic pH was observed for both CeOFA and CeTFS as the catalyst. The evolution of UV-Vis spectra measured during MO photodegradation in the presence of CeOFA is shown in Figure S26. As expected, the shape of the band with a maximum at 465 nm is more complex due to the presence of MO in its deprotonated form (Figure S27). The higher structural complexity is also reflected in the species formed during the degradation. Within the first 15 min of irradiation, the visible band shifts towards larger wavelengths ($\lambda_{max} = 472$ nm), followed by a hypsochromic shift towards 400 nm. These absorption bands are probably due to intermediate structures formed by demethylation, methylation and hydroxylation processes, as reported by Baiocchi et al.[51]

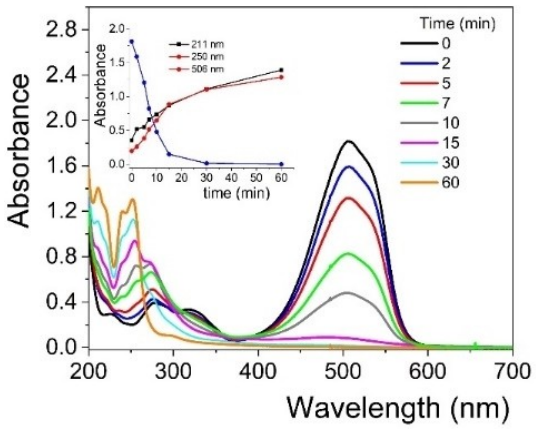


**Figure 6.** Absorption spectra recorded during the photodegradation of MO ($4.0\times10^{-5}$ mol·L$^{-1}$) with CeTFS (1.0 g·L$^{-1}$) in aqueous dispersion at pH 2.5 as a function of irradiation time ($\lambda = 355$ nm). Inset: change in absorbance at 211, 250 and 506 nm as a function of irradiation time.

The degradation kinetics of MO at pH 6.7 could not be determined due to the spectral overlap between MOF and degradation products. The accumulation of intermediates containing azo bonds and their almost complete degradation within 60 minutes (Figure S26) seems to indicate an improved efficiency of MO degradation at pH 6.7. One explanation could be the concentration increase of OH• radicals, generated by oxidation of hydroxyl ions that are more available close to the MOF surface. However, based on the available data we cannot exclude direct oxidation of molecules. As already observed at the more acidic pH, the thermal reaction at pH 6.7 proved to be slower, as demonstrated by the decrease of the visible band absorbance by only 50% after a reaction time of 60 min (Figure S27). To ensure that the degradation was solely due to the presence of MOFs, degradation studies were also carried out in the absence of the MOFs at pH 6.7, both in the dark and under irradiation, and no MO degradation was observed.

Recycling tests at pH 2.5 showed that there was no significant decrease in efficiency after two runs, indicating good stability (Figure S28). This was also confirmed by PXRD (Figure S29) and by quantification of Ce ions on the reaction liquid phase. The PXRD pattern of CeOFA shows no changes in crystallinity, while the long-range order CeTFS decreased. These results are consistent with the concentration of Ce ions measured in the reaction solution. Leaching of cerium ions into solution was quantified with inductively coupled plasma-optical emission spectroscopy (ICP-OES) after 1 h irradiation to 0.5 wt% for CeOFA and 3.0 wt% for CeTFS at pH = 2.5 and to 0.2 wt% for CeOFA and 2.7 wt% for CeTFS at pH = 6.7.

## Conclusions

Two new Ce-MOFs CeTFS and CeOFA with perfluoroalkyl dicarboxylate ions have been prepared under mild reaction conditions and fully characterized by several techniques. Their structures are isoreticular to the zirconium fumarate MOF-801, although the flexibility of the perfluoralkyl linker and the steric hindrance of fluorine resulted in a very low porosity for both compounds. The kinetics of MOF formation and Ce oxidation state were also investigated by a combined *in-situ* XAS and XRD crystallization study using synchrotron radiation. DFT calculations have been used to determine the electronic structure of the Ce-MOFs, which supports their ability to act as hole donors for the production of OH•

radicals and also for the direct oxidation of methyl orange (MO), which was used as an organic model pollutant. Therefore the two Ce-MOFs were used as photocatalysts for the degradation of MO in water at different pH values under UV-Vis irradiation. CeOFA shows good kinetics with minor loss of activity while preserving crystallinity. The recyclability of CeOFA makes it preferable to other homogeneous phase oxidants, which may be more efficient in degradation (such as CAN) but are certainly less environmentally friendly as they are more difficult to recover.

## Supporting Information

The authors have cited additional references within the Supporting Information. CCDC 2323049 contains the crystallographic data for CeTFS and CCDC 2323048 contains the crystallographic data for CeOFA.

## *Acknowledgements*

D. M. V. and N. S. acknowledge financial support by the Deutsche Forschungsgemeinschaft Ce/Zr-MOFs (STO 643/15-1). F. C., M. S. N., and L. T. acknowledge the Italian MUR through the Project PRIN 2020 doMino (ref 2020P9KBKZ). ESRF is acknowledged for provision of beamtime at ID24-DCM beamline (experiment CH-6604). Dr. Cesare Atzori is acknowlwdged for the support during the beamtime. D. M. V., N. R., B. A., and C. M. acknowledge the ESRF for covering the travel and accommodation expenses for this beam time. Dr. Catia Clementi is acknowledged for the UV-Vis measurement. E. M. acknowledges support from Next Generation EU through PRIN PNRR 2022 project "BEAGLE" (P20223HSWX). E. M. and A. A. A. wish to thank the Distinguished Scientist Fellowship Program (DSFP) of King Saud University, Riyadh, Kingdom of Saudi Arabia. Open Access funding enabled and organized by Projekt DEAL.

## *Conflict of Interests*

The authors declare no conflict of interest.

## *Data Availability Statement*

The data that support the findings of this study are available in the supplementary material of this article.

**Keywords:** Cerium · Photo catalysis · In-situ study · DFT calculation · Metal-organic framework

[1] R. Freund, O. Zaremba, G. Arnauts, R. Ameloot, G. Skorupskii, M. Dincă, A. Bavykina, J. Gascon, A. Ejsmont, J. Goscianska et al., *Angew. Chem. Int. Ed.* **2021**, *60*, 23975.
[2] M. Taddei, C. Petit, *Mol. Syst. Des. Eng.* **2021**, *6*, 841.
[3] D. Li, H.-Q. Xu, L. Jiao, H.-L. Jiang, *EnergyChem* **2019**, *1*, 100005.
[4] W. Xu, O. M. Yaghi, *ACS Cent. Sci.* **2020**, *6*, 1348.
[5] S. Mallakpour, E. Nikkhoo, C. M. Hussain, *Coord. Chem. Rev.* **2022**, *451*, 214262.
[6] X. Chen, G. Li, *Inorg. Chem. Front.* **2020**, *7*, 3765.
[7] M. Lammert, M. T. Wharmby, S. Smolders, B. Bueken, A. Lieb, K. A. Lomachenko, D. de Vos, N. Stock, *Chem. Commun. (Camb.)* **2015**, *51*, 12578.
[8] X.-P. Wu, L. Gagliardi, D. G. Truhlar, *J. Am. Chem. Soc.* **2018**, *140*, 7904.
[9] J. Jacobsen, A. Ienco, R. D'Amato, F. Costantino, N. Stock, *Dalton Trans.* **2020**, *49*, 16551.
[10] Z. Hu, Y. Wang, D. Zhao, *Chem. Soc. Rev.* **2021**, *50*, 4629.
[11] D. Chen, Y. Cheng, N. Zhou, P. Chen, Y. Wang, K. Li, S. Huo, P. Cheng, P. Peng, R. Zhang et al., *J. Cleaner Prod.* **2020**, *268*, 121725.
[12] J. Gosch, D. Morelli Venturi, E. Svensson Grape, C. Atzori, L. Donà, F. Steinke, T. Otto, T. Tjardts, B. Civalleri, K. A. Lomachenko et al., *Inorg. Chem.* **2023**, *62*, 5176.
[13] J. H. Lee, S. Jeoung, Y. G. Chung, H. R. Moon, *Coord. Chem. Rev.* **2019**, *389*, 161.
[14] A. Schneemann, V. Bon, I. Schwedler, I. Senkovska, S. Kaskel, R. A. Fischer, *Chem. Soc. Rev.* **2014**, *43*, 6062.
[15] I. Senkovska, V. Bon, L. Abylgazina, M. Mendt, J. Berger, G. Kieslich, P. Petkov, J. Luiz Fiorio, J.-O. Joswig, T. Heine et al., *Angew. Chem. Int. Ed.* **2023**, *62*, e202218076.
[16] S. Wang, N. Xhaferaj, M. Wahiduzzaman, K. Oyekan, X. Li, K. Wei, B. Zheng, A. Tissot, J. Marrot, W. Shepard et al., *J. Am. Chem. Soc.* **2019**, *141*, 17207.
[17] D. Morelli Venturi, F. Costantino, *RSC Adv.* **2023**, *13*, 29215.
[18] D. M. Venturi, M. S. Notari, R. Bondi, E. Mosconi, W. Kaiser, G. Mercuri, G. Giambastiani, A. Rossin, M. Taddei, F. Costantino, *ACS Appl. Mater. Interfaces* **2022**, *14*, 40801.
[19] M. Lammert, C. Glißmann, N. Stock, *Dalton Trans.* **2017**, *46*, 2425.
[20] N. Heidenreich, U. Rütt, M. Köppen, A. K. Inge, S. Beier, A.-C. Dippel, R. Suren, N. Stock, *Rev. Sci. Instrum.* **2017**, *88*, 104102.
[21] M. Newville, *J. Phys. Conf. Ser.* **2013**, *430*, 12007.
[22] C. Prescher, V. B. Prakapenka, *High Pressure Res.* **2015**, *35*, 223.
[23] G. Ashiotis, A. Deschildre, Z. Nawaz, J. P. Wright, D. Karkoulis, F. E. Picca, J. Kieffer, *J. Appl. Crystallogr.* **2015**, *48*, 510.
[24] J. Hutter, M. Iannuzzi, F. Schiffmann, J. VandeVondele, *WIREs Comput. Mol. Sci.* **2014**, *4*, 15.
[25] J. VandeVondele, J. Hutter, *J. Chem. Phys.* **2007**, *127*, 114105.
[26] J. P. Perdew, K. Burke, M. Ernzerhof, *Phys. Rev. Lett.* **1996**, *77*, 3865.
[27] S. Goedecker, M. Teter, J. Hutter, *Phys. Rev. B Condens* **1996**, *54*, 1703.
[28] G. Kresse, J. Hafner, *Physical Rev. B Condens.* **1994**, *49*, 14251.
[29] G. Kresse, J. Furthmüller, *Comput. Mater. Sci.* **1996**, *6*, 15.
[30] K. Hendrickx, D. E. P. Vanpoucke, K. Leus, K. Lejaeghere, A. van Yperen-De Deyne, V. van Speybroeck, P. van der Voort, K. Hemelsoet, *Inorg. Chem.* **2015**, *54*, 10701.
[31] M. Campanelli, T. Del Giacco, F. de Angelis, E. Mosconi, M. Taddei, F. Marmottini, R. D'Amato, F. Costantino, *ACS Appl. Mater. Interfaces* **2019**, *11*, 45031.
[32] P. E. Blöchl, *Physical Rev. B Condens.* **1994**, *50*, 17953.
[33] D. G. A. Smith, L. A. Burns, K. Patkowski, C. D. Sherrill, *J. Phys. Chem. Lett.* **2016**, *7*, 2197.
[34] J. Heyd, G. E. Scuseria, M. Ernzerhof, *J. Chem. Phys.* **2003**, *118*, 8207.
[35] A. Altomare, C. Giacovazzo, A. Guagliardi, A. G. G. Moliterni, R. Rizzi, P.-E. Werner, *J. Appl. Crystallogr.* **2000**, *33*, 1180.
[36] J. Jacobsen, B. Achenbach, H. Reinsch, S. Smolders, F.-D. Lange, G. Friedrichs, D. de Vos, N. Stock, *Dalton Trans.* **2019**, *48*, 8433.
[37] C.-N. Li, S.-M. Wang, Z.-P. Tao, L. Liu, W.-G. Xu, X.-J. Gu, Z.-B. Han, *Inorg. Chem.* **2023**, *62*, 7853.
[38] M. Taddei, R. J. Wakeham, A. Koutsianos, E. Andreoli, A. R. Barron, *Angew. Chem. Int. Ed.* **2018**, *57*, 11706.
[39] C. Atzori, K. A. Lomachenko, J. Jacobsen, N. Stock, A. Damin, F. Bonino, S. Bordiga, *Dalton Trans.* **2020**, *49*, 5794.
[40] G. Socrates, *Infrared and Raman characteristic group frequencies. Tables and charts*, John Wiley & Sons LTD, Chichester [etc.], **2015**.
[41] L. Mayrhofer, G. Moras, N. Mulakaluri, S. Rajagopalan, P. A. Stevens, M. Moseler, *J. Am. Chem. Soc.* **2016**, *138*, 4018.
[42] S. Trasatti, *Pure Appl. Chem.* **1986**, *58*, 955.
[43] R. G. Sandberg, G. H. Henderson, R. D. White, E. M. Eyring, *J. Phys. Chem.* **1972**, *76*, 4023.
[44] C. Nançoz, G. Licari, J. S. Beckwith, M. Soederberg, B. Dereka, A. Rosspeintner, O. Yushchenko, R. Letrun, S. Richert, B. Lang et al., *Phys. Chem. Chem. Phys.* **2018**, *20*, 7254.

[45] Y.-H. Chiu, T.-F. Chang, C.-Y. Chen, M. Sone, Y.-J. Hsu, *Catalysts* **2019**, *9*, 430.
[46] A. Dhakshinamoorthy, Z. Li, H. Garcia, *Chem. Soc. Rev.* **2018**, *47*, 8134.
[47] J. L. WANG, J. I. N. Le Xu, *Crit. Rev. Environ. Sci. Technol.* **2012**, *42*, 251.
[48] S. Zbaida, W. G. Levine, *Chem. Res. Toxicol.* **1991**, *4*, 82.
[49] J. Zhong, Y. Zhao, L. Ding, H. Ji, W. Ma, C. Chen, J. Zhao, *Appl. Catal. B* **2019**, *241*, 514.
[50] D. A. Armstrong, R. E. Huie, S. Lymar, W. H. Koppenol, G. Merényi, P. Neta, D. M. Stanbury, S. Steenken, P. Wardman, *BioInorg. React. Mech.* **2013**, *9*, 1594.
[51] C. Baiocchi, M. C. Brussino, E. Pramauro, A. B. Prevot, L. Palmisano, G. Marì, *Int. J. Mass Spectrom.* **2002**, *214*, 247.

Manuscript received: January 31, 2024
Accepted manuscript online: April 3, 2024
Version of record online: ■■, ■■

# RESEARCH ARTICLE

Ligand-to-metal charge transfer potential for photodegradation of organic dyes in new perfluorinated Ce-MOFs.

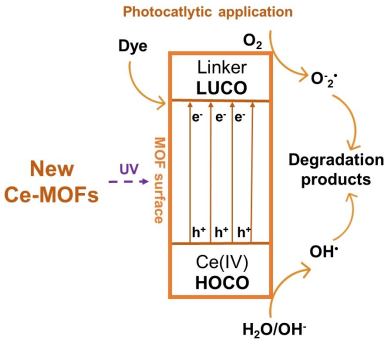


*Dr. D. Morelli Venturi, M. Sole Notari, L. Trovarelli, Dr. E. Mosconi, A. A. Alothman, Dr. A. Molokova, N. Ruser, C. Meier, B. Achenbach, Dr. K. A. Lomachenko, Prof. T. del Giacco*, Prof. F. Costantino*, Prof. Dr. N. Stock**

1 – 10

**Synthesis, Structure and (Photo)Catalytic Behavior of Ce-MOFs Containing Perfluoroalkyl-carboxylate Linkers: Experimental and Theoretical Insights**